Self-Organized Growth, Structure, and Magnetism of Monatomic Transition-Metal Oxide Chains

Pascal Ferstl, Lutz Hammer, Christopher Sobel, Matthias Gubo, Klaus Heinz, and M. Alexander Schneider
Lehrstuhl für Festkörperphysik, Friedrich-Alexander Universität Erlangen-Nürnberg, Staudtstrasse 7, D-91058 Erlangen, Germany

Florian Mittendorfer and Josef Redinger
Institut für Angewandte Physik and Center for Computational Materials Science, Technische Universität Wien, Wiedner Hauptstrasse 8-10/134, A-1040 Vienna, Austria

(Received 31 May 2016; published 21 July 2016)

We report on the self-organized growth of monatomic transition-metal oxide chains of (3×1) periodicity and unusual MO_2 stoichiometry (M = Ni, Co, Fe, Mn) on Ir(100). We analyze their structural and magnetic properties by means of quantitative LEED, STM, and density functional theory (DFT) calculations. LEED analyses reveal a fascinating common atomic structure in which the transition-metal atoms sit above a missing-row structure of the surface and are coupled to the substrate only via oxygen atoms. This structure is confirmed by DFT calculations with structural parameters deviating by less than 1.7 pm. The DFT calculations predict that the NiO_2 chains are nonmagnetic, CoO_2 chains are ferromagnetic, while FeO_2 and MnO_2 are antiferromagnetic. All structures show only weak magnetic interchain coupling. Further, we demonstrate the growth of oxide chains of binary alloys of Co and Ni or Fe on Ir(100), which allows us to produce well-controlled ensembles of ferromagnetic chains of different lengths separated by nonmagnetic or antiferromagnetic segments.

DOI: 10.1103/PhysRevLett.117.046101

In a variety of quasi-one-dimensional systems exciting electronic [1–5], magnetic [6–8], and chemical properties [9,10] were reported. Such systems can be produced using one of three options: first, the atom-by-atom assembly [5–7], second, decoration of substrate step edges [8–11], and third, self-assembled growth [1–4,12]. Atom-by-atom assembly results in the utmost control over the low-dimensional structures, but it does not allow their production on any larger scale. Step decoration is the most flexible if it comes to the choice of materials; however, the system length can hardly be controlled. This is due to the fact that step edges exhibit kinks and also serve as preferred nucleation centers of residual contaminants. Lastly, self-assembled growth is limited to certain choices of materials, but one can produce one-dimensional structures to high perfection and with high surface density. This opens the opportunity to employ spatially averaging methods to determine their properties. Low-dimensional metal oxide structures in general [13] and as quasi-one-dimensional systems [14] have been reviewed, although the latter is mainly a theoretical review for lack of experimental realizations.

In this Letter we report on the growth of quasi-one-dimensional metal oxide chains of MO_2 stoichiometry (M = Ni, Co, Fe, Mn) that form self-organized on the Ir(100) surface. The up to 500 atoms long chains form well-ordered (3×1) superstructures and therefore are of much higher lateral density than feasible by the step decoration technique. We resolve the atomic structure of the oxide chains, which is unprecedented in the crystallographic sense for such systems: the transition-metal atoms reside above a missing-row structure with only indirect interaction with the substrate via oxygen atoms. We further discuss the implication of this unusual structure on the electronic and magnetic properties of the chains. To that end, we apply quantitative low-energy electron diffraction (LEED), scanning tunneling microscopy (STM), and density functional theory (DFT).

The samples were prepared in an UHV chamber (pressure in the low 10^{-10} mbar regime) equipped with the typical appliances for surface preparations and a LEED setup. Samples were transferred *in situ* to a room-temperature STM operating at a pressure of 2×10^{-11} mbar. For the LEED structural analyses we collected a database of 10–22 keV intensity data (LEED-IV) for each structure. Full-dynamical LEED spectra were calculated using the phase shifts provided by Rundgren's program [15]. A structural search procedure [16] using the TENSERLEED code [17] was applied controlled by the Pendry R factor [18] for the quantitative comparison of spectra. The DFT calculations were performed with the Vienna *Ab initio* Simulation Package (VASP) [19,20], using projector augmented wave potentials [21] and the Perdew-Burke-Ernzerhof exchange-correlation functional [22] combined with DFT + U corrections [23] with a value of $U - J =$ 1.5 eV. All spatial positions from the DFT calculations were

scaled by approximately 1% to match the calculated substrate lattice parameters with the experimental ones. Details of the experimental and theoretical procedures are given in the Supplemental Material [24].

On Ir(100) the quasi-one-dimensional oxide chains are homogeneously formed when depositing 0.33 ML of the respective transition metal under UHV conditions either on the Ir(100)-(2×1)-O [31] or on the metastable Ir(100)-(1×1) [32] followed by annealing in 1×10^{-7} mbar O_2. The optimum annealing temperatures were determined by LEED via an assessment of the quality of the superstructure spots to $T_{\mathrm{Ni,Co,Fe}} = 970\,\mathrm{K}$ and $T_{\mathrm{Mn}} = 1070\,\mathrm{K}$. When heating the samples beyond these temperatures, oxygen desorbs and the (3×1) phases are destroyed.

The LEED pattern in Fig. 1(a) and the STM overview image [Fig. 1(b)] demonstrate the resulting homogeneity of the surface structure for the case of CoO_2 chains on Ir(100). Perfectly ordered domains with two equivalent, orthogonal orientations are found built up by defect-free monatomic chains of up to 500 atoms length. From atomically resolved STM images [Fig. 1(c)] and from the metal coverage, it can be deduced that the bright protrusions are the Co atoms while the oxygen is not visible. This interpretation is confirmed by our DFT simulations [Fig. 1(c), inset]. The other MO_2 chains look identical in STM (cf. Ref. [24]).

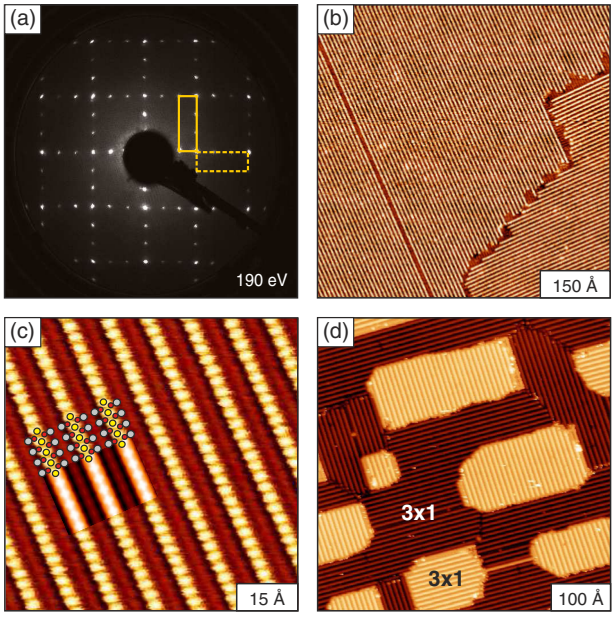

FIG. 1. (3×1) CoO_2 structure on Ir(100). (a) LEED pattern showing the (3×1) structure annealed at 970 K with two orthogonal domains. (b) Corresponding large scale STM image taken at room temperature. (c) Atomically resolved STM image showing monatomic chains in (3×1) periodicity. Inset: DFT simulation of the STM image. (d) Large scale STM image of a preparation annealed only at 670 K. The (3×1) structure is still homogeneously formed but islands are observed that cover one-third of the surface area.

Figure 1(d) shows the situation obtained when annealing the CoO_2 chains to a lower temperature of 670 K. Under these conditions the complete surface is covered by the same (3×1) phase found at the optimal annealing temperature. But in contrast to the ideal flat domains of the preparation of Fig. 1(b), one-third of the surface is covered by monolayer high adislands corresponding exactly to the areal density of evaporated Co. This proves that the newly formed (3×1) phase is not simply an adsorbate phase on the intact Ir(100) surface but is formed by a one-to-one exchange of Ir substrate atoms by Co. Hence, for the ideal morphology of Fig. 1(b), relatively high temperatures are needed to dissolve the (3×1) CoO_2 islands by diffusion of the exchanged Ir atoms to step edges. It was also possible to grow the (3×1) CoO_2 structure on Pt(100) but not on the (100) surfaces of Cu, Ag, Au, Pd, or Rh. The preparation recipe was also tested with Cu and Ti on Ir(100); both metals did not form the quasi-one-dimensional structure.

In order to resolve the crystallographic structure of the (3×1) chain phase, structure determinations were carried out for all systems by full-dynamical LEED intensity analyses and compared to the relaxed structures as determined by DFT. Complete LEED-IV analyses were mandatory for all MO_2 systems since the experimental spectra of the fractional order beams taken from phases with different transition-metal ions differed substantially (R factors $R > 0.6$) although the final structures turned out to be quite similar (cf. Ref. [24]).

Several types of models were tested during the LEED analysis. Only the models presented in Fig. 2 produced a convincing best fit between experimental and calculated spectra. By optimization of 20 geometrical and 3 vibrational parameters the LEED analyses yielded convincing R factors in the range $R = 0.08$–0.10, while the best-fit values of all other tested models were $R > 0.4$. An example of the fit quality is shown in Fig. 2(a) for two beams; the full data sets are presented in Ref. [24]. The relevant crystallographic features of the best-fit structure for the case of CoO_2 is schematically displayed in Fig. 2(b) top and Fig. 2(c) side view. In Fig. 2(d) we show the position of the transition-metal ion for the remaining MO_2 structures on Ir(100). Each transition-metal atom M is coordinated to four surrounding oxygen atoms, which in turn are bound to one substrate Ir atom and two M atoms. An essential and fascinating aspect of all MO_2 structures is that the M atoms nominally replace a surface iridium row consistent with the experimental findings shown in Fig. 1(d). However, the transition-metal rows are shifted by half a substrate lattice vector along the chain and pulled out of the Ir surface layer by the M-O bonds [Figs. 2(b) and 2(c)]. Consequently, substantial atomic relaxations are induced in the Ir substrate. Comparing the different systems we find that in the series Ni, Co, Fe, the M atom sinks farther into the trough of the missing Ir row ($d_{\mathrm{Ni}} > d_{\mathrm{Co}} > d_{\mathrm{Fe}}$) while the oxygen atoms hardly change their position with respect to the Ir

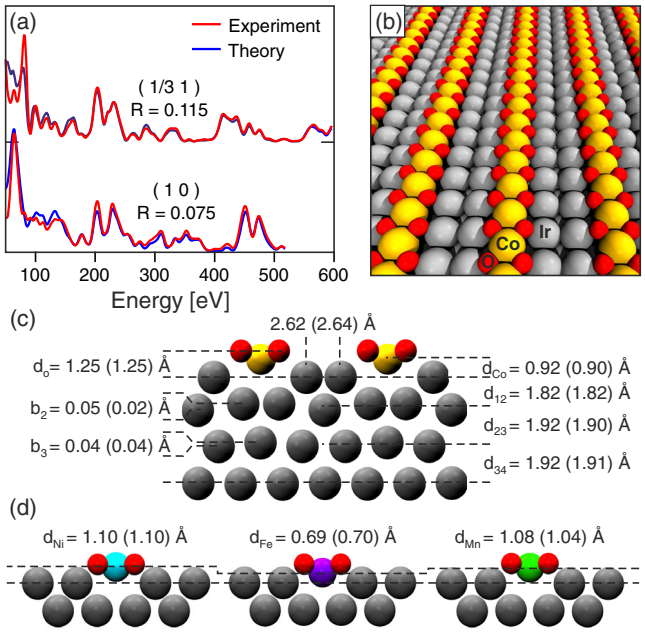

FIG. 2. Structures as derived from LEED. (a) Example of the close correspondence between experimental and theoretical LEED intensity for the proposed structural model. (b) Top and (c) side view of the (3×1) CoO_2 structure. (d) Side views of the MnO_2, FeO_2, and NiO_2 structures on Ir(100). The most important structural parameters are given as derived from experiment and DFT calculations (in brackets). DFT values were scaled as described in the text.

substrate [Figs. 2(c) and 2(d)]. Surprisingly, the MnO_2 chains do not follow this trend and show a $d_{\mathrm{Mn}} \approx d_{\mathrm{Ni}}$. From the structural data nearest neighbor M-Ir distances $d_{M\text{-Ir}}$ follow that are larger by at least 0.3 Å than the corresponding bond lengths (Table I); hence, no M-Ir bonding is expected. The M-M bond length of 2.71 Å ($= a_{\mathrm{Ir}}$) is larger than that of the corresponding bulk metal but smaller than that of the bulk oxide. The whole structure may be understood as a (3×1) periodic missing-row structure of Ir(100) induced by the MO_2 chains which cover the created troughs avoiding direct M-Ir bonding.

TABLE I. Parameters of (3×1) MO_2 structures on Ir(100) from the DFT calculations: $d_{M\text{-Ir}}$ is the shortest distance between the M atom and substrate Ir atoms (in the second layer), μ_M is the magnetic moment (in units of Bohr magnetons μ_B), n_d is the number of transition-metal d electrons, q_M the charge of the transition-metal atom, q_{O} and q_{Ir} the charges of the O and Ir atoms of the first surface layer (in units of the elementary charge e). Lengths from DFT calculations were scaled as described in the text.

	$d_{M\text{-Ir}}$ (Å)	μ_M (μ_B)	n_d (e)	q_M (e)	q_{O} (e)	q_{Ir} (e)
NiO_2	3.22	0.00	8.4	+1.00	−0.81	+0.29
CoO_2	3.02	1.96	7.2	+1.14	−0.84	+0.28
FeO_2	2.83	3.55	6.0	+1.37	−0.89	+0.27
MnO_2	3.12	3.62	4.9	+1.53	−0.97	+0.24

The DFT calculations reproduce the LEED best-fit structures and the STM images to an excellent degree of accuracy. The root mean square deviation between the structural parameters from the LEED analyses and from the DFT calculations is less than 1.7 pm for all structures. This demonstrates the reliability of the two methods but also serves as incentive to analyze the properties of the MO_2 chains predicted by DFT. The calculations show that the NiO_2 chains are nonmagnetic while the other MO_2 chains carry a large magnetic moment on the metal ion (cf. Table I). It is found that in CoO_2 a ferromagnetic coupling along the chains is favorable by 25 meV, while for FeO_2 and MnO_2 the antiferromagnetic coupling is favored by 44 and 27 meV per M atom, respectively. The magnetic coupling energy per M atom across the chains was calculated in a 6×2 cell and found to be ferromagnetic for Co (4 meV) and antiferromagnetic for Fe (9 meV) and Mn (0.4 meV). Therefore, the chains can be considered as nearly one-dimensional magnetic objects, where the strength of residual magnetic coupling across the chains is obviously connected to the M-Ir distance (Table I). A Bader analysis [33] shows that the charge states of the transition-metal atoms is between +1.0 (Ni) and +1.5 (Mn), considerably less than one would naively expect from the formal stoichiometry of the chains (Table I). However, this finding is easily rationalized by the additional binding of the O atoms to the substrate, yielding an O charge around −1.0 and a slight positive charge on the bonded Ir atoms in the topmost layer. Any remaining charge deficit is compensated by a corresponding charge in the second Ir layer. Comparing the number of d electrons n_d and the charge states q_M, one finds a non-negligible contribution of transition metal s and p electrons to the total charge. This affects the on-site screening of the d electrons, which in turn justifies the choice of a rather low value of the Hubbard U.

Figure 3 shows the calculated projected density of states (PDOS) of the four MO_2 chains with the coordinate system chosen such that the x axis is oriented along the M-O bond (along [010]). As a common feature of the MO_2 oxide chains, the calculations show a pronounced bonding or antibonding splitting of the $d_{x^2-y^2}$ states due to the $pd\sigma$ interaction with the oxygen p states. Yet, there is also a major difference between NiO_2 [Fig. 3(a)] and the other three oxide chains: NiO_2 is nonmagnetic, while the magnetic splitting is around 2 eV for CoO_2 and 4–5 eV for FeO_2 and MnO_2, reflecting the trend of the magnetic moments (see Table I). While FeO_2 and MnO_2 are predicted to be antiferromagnetic and have a magnetic moment close to the DFT values of the respective MO bulk oxides, we find a reduced moment and a different magnetic coupling for CoO_2 and no moment for NiO_2. The breakdown of the magnetic moment in the case of NiO_2 is due to the pronounced $pd\sigma$ interaction overturning the magnetic splitting. The height variation of the M atoms is connected

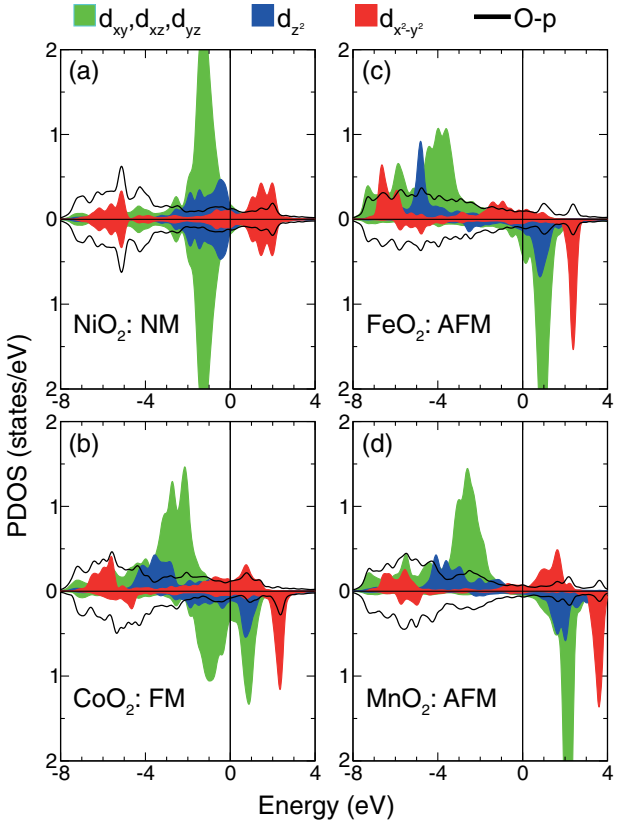

FIG. 3. Partial density of states (PDOS) for the Ir(100)-(3×1)-MO_2 phases calculated in a 3×1 super cell on a 7 layer Ir substrate. The filled curves correspond to the M-$d_{x^2-y^2}$, the M-d_{z^2}, and the summed M-d_{xy}, d_{xz}, d_{yz} contributions, respectively (colors, see figure). The black line denotes the O-p contribution. NM (a), FM (b), and AFM (c,d) indicate a nonmagnetic, a ferromagnetic, and an antiferromagnetic ground state with collinear ordering, respectively.

to the M-O bond strength, which in turn is determined by the occupancy of the bonding and antibonding $pd\sigma$ orbitals. While the antibonding states are unoccupied for NiO_2, the exchange splitting increases the antibonding contribution by pulling down states in the majority spin channel and it furthermore decreases the bonding contribution in the minority channel for CoO_2 and FeO_2. This leads to an increase in the M-O bond length from 1.86 Å (Ni) to 1.94 Å (Fe) and hence a decrease in the height from 1.10 Å (Ni) to 0.70 Å (Fe) [Fig. 2]. For Mn this series is broken because the antibonding orbitals are again unoccupied due to d-band filling: compared to Fe, the number of d electrons is reduced by one and, therefore, the Mn $d_{x^2-y^2}$ states are almost rigidly shifted up in energy [Fig. 3(d)]. Hence, the Mn-O bond is shortened to 1.90 Å, and the Mn height increased to 1.04 Å.

We found that alloy oxide chains can also be produced from a mixture of two transition-metal species. Because of the different magnetic properties of the MO_2 chains, this opens the possibility of forming complex magnetic structures where ferromagnetic segments are separated by antiferromagnetic or nonmagnetic segments. As an example, the resulting structure of $Co_{0.5}Ni_{0.5}O_2$ and of $Co_{0.67}Ni_{0.33}O_2$ chains is shown in Fig. 4(a). The chemical identity of the atoms in the chain can clearly be visualised by STM for the chosen examples [Figs. 4(a) and 4(b)]. From the STM images the resulting probability $P(n)$ of an M atom to reside in a chain segment of length n was determined and is plotted in Fig. 4(c) for three different M contents x. We find $P(n)$ agrees with the expectation of a statistical incorporation of the transition-metal atoms into the growing alloy oxide chains. We note that $P(n)$ is equivalent to the weight of the signal from an n chain in a spatially averaging experiment like XMCD [8].

In conclusion, we have presented a novel system where monatomic transition-metal MO_2 chains are grown by self-assembly on the Ir(100) surface. We performed crystallographic analyses of in total four structures which so far could not be achieved with similar systems grown, e.g., at step edges. We find an excellent quantitative agreement between the experimentally determined structures and the fully relaxed ones from first-principles DFT calculations. From the latter we derived the electronic and magnetic properties of the MO_2 chains and found them to be close to magnetically one dimensional. The magnetic coupling along the chains is predicted to be nonmagnetic for NiO_2, ferromagnetic for CoO_2, and antiferromagnetic for FeO_2 and MnO_2 chains. We further showed that alloy oxide

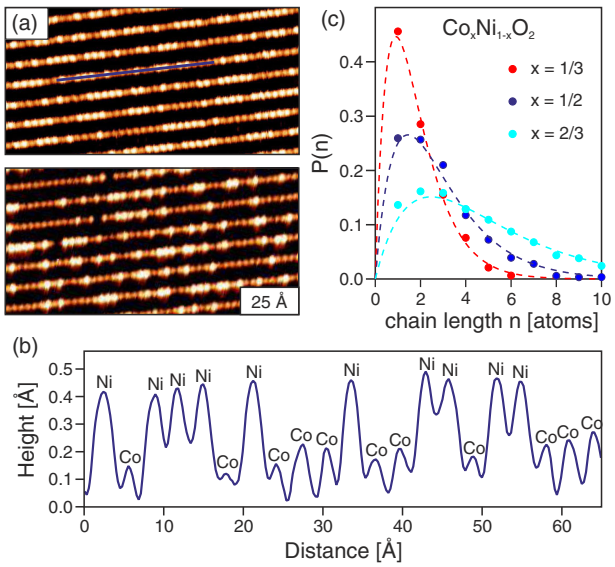

FIG. 4. (a) Atomically resolved STM image of $Co_{0.5}Ni_{0.5}O_2$ (upper panel) and $Co_{0.67}Ni_{0.33}O_2$ chains (lower panel). (b) Line section along the line indicated in (a). The two species are easily identified. (c) Analysis of the probability $P(n)$ of an M atom to reside in a chain segment of length n as a function of different M content x of the alloy oxide. The experimental data (symbols) follow closely the expectation (lines) according to a random incorporation of the metal atoms.

chains of statistical mixtures of Ni, Co, and Fe can also be grown. These alloy oxide chains represent a well-controlled ensemble of mixed one-dimensional (anti)ferromagnetic magnets with nonmagnetic separators.

The authors are grateful for financial support by the Deutsche Forschungsgemeinschaft (DFG) (COMCAT) and the Austrian Science Fund (FWF) (SFB FOXSI F4511-N16), and for the computer support of the Vienna Scientific Cluster (VSC).

[1] H. W. Yeom, S. Takeda, E. Rotenberg, I. Matsuda, K. Horikoshi, J. Schaefer, C. M. Lee, S. D. Kevan, T. Ohta, T. Nagao, and S. Hasegawa, Phys. Rev. Lett. **82**, 4898 (1999).
[2] F. J. Himpsel, K. N. Altmann, R. Bennewitz, J. N. Crain, A. Kirakosian, J.-L. Lin, and J. L. McChesney, J. Phys. Condens. Matter **13**, 11097 (2001).
[3] H. J. W. Zandvliet, A. van Houselt, and B. Poelsema, J. Phys. Condens. Matter **21**, 474207 (2009).
[4] J. Aulbach, J. Schäfer, S. C. Erwin, S. Meyer, C. Loho, J. Settelein, and R. Claessen, Phys. Rev. Lett. **111**, 137203 (2013).
[5] S. Fölsch, P. Hyldgaard, R. Koch, and K. H. Ploog, Phys. Rev. Lett. **92**, 056803 (2004).
[6] C. F. Hirjibehedin, C. P. Lutz, and A. J. Heinrich, Science **312**, 1021 (2006).
[7] S. Loth, S. Baumann, C. P. Lutz, D. M. Eigler, and A. J. Heinrich, Science **335**, 196 (2012).
[8] P. Gambardella, A. Dallmeyer, K. Maiti, M. C. Malagoli, W. Eberhardt, K. Kern, and C. Carbone, Nature (London) **416**, 301 (2002).
[9] S. Surnev, F. Allegretti, G. Parteder, T. Franz, F. Mittendorfer, J. N. Andersen, and F. P. Netzer, Chem Phys Chem **11**, 2506 (2010).
[10] J. Schoiswohl, F. Mittendorfer, S. Surnev, M. G. Ramsey, J. N. Andersen, and F. P. Netzer, Phys. Rev. Lett. **97**, 126102 (2006).
[11] P. Gambardella, M. Blanc, H. Brune, K. Kuhnke, and K. Kern, Phys. Rev. B **61**, 2254 (2000).
[12] C. Giovanardi, A. Klein, A. Schmidt, L. Hammer, and K. Heinz, Phys. Rev. B **78**, 205416 (2008).
[13] S. Surnev, A. Fortunelli, and F. P. Netzer, Chem. Rev. **113**, 4314 (2013).
[14] C. Noguera and J. Goniakowski, J. Chem. Phys. **139**, 084703 (2013).
[15] J. Rundgren, Phys. Rev. B **68**, 125405 (2003).
[16] M. Kottcke and K. Heinz, Surf. Sci. **376**, 352 (1997).
[17] V. Blum and K. Heinz, Comput. Phys. Commun. **134**, 392 (2001).
[18] J. B. Pendry, J. Phys. C **13**, 937 (1980).
[19] G. Kresse and J. Hafner, Phys. Rev. B **47**, 558 (1993).
[20] G. Kresse and J. Furthmüller, Comput. Mater. Sci. **6**, 15 (1996).
[21] G. Kresse and D. Joubert, Phys. Rev. B **59**, 1758 (1999).
[22] J. P. Perdew, K. Burke, and M. Ernzerhof, Phys. Rev. Lett. **77**, 3865 (1996).
[23] S. L. Dudarev, G. A. Botton, S. Y. Savrasov, C. J. Humphreys, and A. P. Sutton, Phys. Rev. B **57**, 1505 (1998).
[24] See Supplemental Material at http://link.aps.org/supplemental/10.1103/PhysRevLett.117.046101, which includes Refs. [25–30], for experimental and theoretical procedures, the details and data of the LEED analyses, further STM data, and a compilation of all structural parameters.
[25] K. Heinz, Rep. Prog. Phys. **58**, 637 (1995).
[26] P. J. Rous, J. B. Pendry, D. K. Saldin, K. Heinz, K. Müller, and N. Bickel, Phys. Rev. Lett. **57**, 2951 (1986).
[27] J. W. Arblaster, Platinum Met. Rev. **54**, 93 (2010).
[28] C. Tröppner, T. Schmitt, M. Reuschl, L. Hammer, M. A. Schneider, F. Mittendorfer, J. Redinger, R. Podloucky, and M. Weinert, Phys. Rev. B **86**, 235407 (2012).
[29] F. Mittendorfer, M. Weinert, R. Podloucky, and J. Redinger, Phys. Rev. Lett. **109**, 015501 (2012).
[30] M. Gubo, C. Ebensperger, W. Meyer, L. Hammer, K. Heinz, F. Mittendorfer, and J. Redinger, Phys. Rev. Lett. **108**, 066101 (2012).
[31] P. Ferstl, T. Schmitt, M. A. Schneider, L. Hammer, A. Michl, and S. Müller, Phys. Rev. B **93**, 235406 (2016).
[32] J. Küppers and H. Michel, Appl. Surf. Sci. **3**, 179 (1979).
[33] R. F. W. Bader, Chem. Rev. **91**, 893 (1991).